The Nearby Luminous Transient AT2018cow: A Magnetar Formed in a Subrelativistically Expanding Nonjetted Explosion

P. Mohan[1] , T. An[1,2] , and J. Yang[3,1]

[1] Shanghai Astronomical Observatory, 80 Nandan Road, Shanghai 200030, People's Republic of China; pmohan@shao.ac.cn, antao@shao.ac.cn
[2] Key Laboratory of Radio Astronomy, Chinese Academy of Sciences, 210008 Nanjing, People's Republic of China
[3] Department of Space, Earth and Environment, Chalmers University of Technology Onsala Space Observatory, SE-439 92 Onsala, Sweden

Abstract

The fast-rising blue optical transient AT2018cow indicated unusual early-phase characteristics unlike relatively better studied explosive transients. Its afterglow may be produced by either a relativistically beamed (jetted) or intrinsically luminous (nonjetted) ejecta and carries observational signatures of the progenitor and environment. High-resolution monitoring can distinguish between these scenarios and clarify the progenitor nature. We present very long baseline interferometry (VLBI) observations of AT2018cow at 5 GHz involving 21 radio telescopes from the European VLBI Network with five sessions spanning ≈ 1 yr. With an astrometric precision up to 25 μas per epoch, the rapidly fading compact mas-scale source is found to be nonjetted with a proper motion of $\leqslant 0.15$ mas yr^{-1} (0.14 c). This and a dense (number density $\approx 10^4$–10^5 cm^{-3}) magnetized environment (magnetic field strength $\geqslant 0.84$ G) are characteristic of a newly formed magnetar driven central engine, originating in the successful explosion of a low-mass star.

Unified Astronomy Thesaurus concepts: Transient sources (1851); High energy astrophysics (739); Very long baseline interferometry (1769); Magnetars (992); Burst astrophysics (187)

1. Introduction

Transient astrophysical events are increasingly detected by optical and high-energy (X-rays, gamma-rays) survey telescopes (e.g., Drout et al. 2014; Inserra 2019). Owing to advances in data collection and processing, their identification is near real-time with follow-up monitoring observations being triggered within a few hours. These events are generally indicative of cataclysmic cosmic explosions. They involve the core collapse of a massive star or merger of two stars (e.g., supernovae and gamma-ray bursts), or the tidal disruption of a star by a massive black hole. Fast-rising blue optical transients (FBOTs) are characterized by a rapid rise to a peak (timescale of $\leqslant 10$ days, luminosity of 10^{43}–10^{44} erg s^{-1}) or a time above half-maximum of the luminosity $t_{1/2} \leqslant 12$ days and a strongly blue color ($g-r < -0.2$) near the peak following which is an exponential decline within 30 days (e.g., Pursiainen et al. 2018; Inserra 2019). Their origin and progenitors are poorly understood mainly due to the current lack of dedicated multiwavelength monitoring observations. The FBOT AT2018cow was identified in the Asteroid Terrestrial-impact Last Alert System (ATLAS) survey on 2018 June 16 (Smartt et al. 2018), hosted in the dwarf spiral galaxy CGCG 137-068 at a redshift of 0.014 (Prentice et al. 2018). It shows peculiar properties: the fastest rise with a timescale <3.3 days, a $t_{1/2}$ of <1.7 days (during the rising phase), a high peak luminosity of $(1.7 - 4.0) \times 10^{44}$ erg s^{-1} (exceeding that of superluminous supernovae), and an unusual featureless non-evolving early-phase spectrum (Prentice et al. 2018) followed by a rapid decline in the light curve (Prentice et al. 2018; Margutti et al. 2019; Perley et al. 2019). This made it one of the most extreme among the current sample of FBOTs and thus presented a unique opportunity for the continued monitoring to help clarify its origin and physical properties.

Multiwavelength studies of AT2018cow mostly probed the early optically thick rising phase of spectral evolution (Prentice et al. 2018; Rivera Sandoval et al. 2018; Ho et al. 2019; Kuin et al. 2019; Margutti et al. 2019; Perley et al. 2019). Optical spectroscopy indicates a peak blackbody temperature of $\approx 27,000$ K, ejecta mass of 0.1–0.4 $M_\odot$ and a transition from an initial featureless spectrum to the appearance of distinct broad H and He emission lines only after 15 days from the discovery (Prentice et al. 2018; Margutti et al. 2019; Perley et al. 2019). The early X-ray flux was variable over day timescales, suggestive of a shock interacting with a nonuniform surrounding medium (Margutti et al. 2019). The early-phase self-absorbed radio emission is indicative of an energetic interaction with a dense medium (number density of 3×10^4–4×10^5 cm^{-3}; Ho et al. 2019). A powering by the radioactive decay of ^{56}Ni, expected in core-collapse supernovae, was ruled out based on a nonphysical requirement on the Ni mass (≈ 3 $M_\odot$) in comparison to the inferred ejecta mass of ≈ 0.1–0.4 $M_\odot$ and the inability to account for the light-curve decay (Prentice et al. 2018). Powering by the tidal disruption of a white dwarf star by an intermediate-mass black hole ($10^4 M_\odot$; Kuin et al. 2019; Perley et al. 2019) was disfavored owing to a dense (Ho et al. 2019; Margutti et al. 2019) highly magnetized (Huang et al. 2019) environment inferred in the immediate vicinity of the transient, which may be challenging to naturally develop in this scenario and require a preexisting reservoir (Margutti et al. 2019). The absence of excitation H and He narrow lines following the transition from a high-velocity expansion ($\geqslant 0.1c$) to a slower one (≈ 0.02 c) seem to disfavor an origin in a failed regular supernovae of a giant star (with a consequent direct collapse to a black hole; Perley et al. 2019).

These multiwavelength studies find evidence for a central engine consisting of a compact object (newly formed stellar-mass black hole or neutron star/magnetar) powering the early phase of the source through accretion-jet/outflow production and sustenance (Ho et al. 2019; Huang et al. 2019; Lyutikov & Toonen 2019; Margutti et al. 2019). The polar directed outflow

<div align="center">
Table 1
The Experiment Setup for the EVN Observations of AT2018cow
</div>

Session	Project Code	Date yy mm dd	ν_{obs} (GHz)	Time (hr)	BW (Mbps)	Radio Telescopes
1	RY007A	18 Sep 18	1.66	2.0	1024	Jb2, Wb, Ef, Mc, On85, Tr, Sr, Cm, De, Kn
2	RY007B	18 Oct 20	4.99	12.0	1024	Jb2, Wb, Ef, Mc, On85, Ur, Tr, Ys, Hh, Sv, Zc, Bd, Ib, Ar, Km
	RY007C	18 Oct 21	4.99	12.0	1024	Jb2, Wb, Ef, Mc, On85, Ur, Tr, Ys, Hh, Sv, Zc, Bd, Ib, Ar, Km
3	EY033A	19 Feb 15	4.93	3.0	2048	Jb2, Ef, Nt, Mc, On85, Tr, Ys, Hh, Ib
4	EY033B	19 Mar 5	4.99	12.0	1024	Jb2, Wb, Ef, Mc, Nt, On85, T6, Ur, Tr, Ys, Hh, Sv, Zc, Bd, Ib
	EY033C	19 Mar 6	4.99	12.0	1024	Jb2, Wb, Ef, Mc, Nt, On85, T6, Ur, Tr, Ys, Hh, Sv, Zc, Bd, Ib
5	EM137	19 Jun 5	4.93	12.0	2048	Jb2, Wb, Ef, Mc, Nt, On85, T6, Tr, Ys, Hh, Sv, Zc, Bd, Ir

Note. Columns give (1) Session ID, (2) EVN project code, (34) observing date and frequency, (56) total observing time and recording bandwidth, and (7) a total of 21 participating radio telescopes: Ar (Arecibo 300 m, USA), Bd (Badary 32 m, Russia), Cm (Cambridge 32 m, UK), De (Defford 25 m, UK), Ef (Effelsberg 100 m, Germany), Hh (Hartebeesthoek 26 m, South Africa), Ib (Irbene 32 m, Latvia), Ir (Irbene 16 m, Latvia), Jb2 (Lovell 76 m, UK), Km (Kunming 40 m, China), Kn (Knockin 25 m, UK), Mc (Medicina 25 m, Italy), On85 (Onsala 25 m, Sweden), Sr (Sardinia 64 m, Italy), Sv (Svetloe 32 m, Russia), T6 (Tianma 65 m, China), Tr (Torun 32 m, Poland), Ur (Urumqi 26 m, China), Wb (Westerbork 25 m, Netherlands), Ys (Yebes 40 m, Spain), Zc (Zelenchukskaya 32 m, Russia).

(Margutti et al. 2019; Soker et al. 2019) interacts with the dense, stratified medium (Rivera Sandoval et al. 2018) producing the observed flux density evolution and variability (Rivera Sandoval et al. 2018; Ho et al. 2019). There is then the possibility of discovering a collimated relativistic jet with Doppler-boosted emission if it can be sustained by the central engine. However, a recent very long baseline interferometry (VLBI) study of AT2018cow (spanning up to 287 days after discovery) at 22 and 8.4 GHz finds a symmetric expansion with proper motion constrained to $\leqslant 0.51\ c$ and suggests that the jet may not be long lived (Bietenholz et al. 2020), thus requiring confirmation.

The luminous afterglow emission in AT2018cow carries observational signatures of the progenitor and environment. High-resolution monitoring can help pin down the transient origin through inferred physical properties and stringent constraints on proper motion. This can be accomplished with VLBI imaging, which has been used in the past to understand the structure and environment of gamma-ray bursts (Taylor et al. 2004; Ghirlanda et al. 2019) and tidal disruption events (Yang et al. 2016). The obtained information from VLBI observations is crucial in localizing the afterglow and inferring if it is jetted/collimated or nonjetted/wide-angled, constraining the explosion energy, number density, and distribution of the surrounding medium.

We report our imaging observations of AT2018cow over five sessions (between t_d of 94 and 355 days after discovery) using the European VLBI Network (EVN), conducted at 5 GHz to ensure a detection over a long duration. As these observations cover the turnover and late optically thin spectral evolution phase, they provide unique information to discern the source nature, especially as the source faded rapidly rendering it challenging for other multiwavelength instruments to capture. With the cosmological parameters $H_0 = 70\ \mathrm{km\ s^{-1}\ Mpc^{-1}}$, $\Omega_m = 0.27$, $\Omega_\Lambda = 0.73$, an angular size of 1 mas corresponds to a projected size of 0.286 pc at $z = 0.014$ (Wright 2006) and a proper motion speed of 1 mas yr^{-1} corresponds to 0.93 c.

2. Observations and Data Processing

2.1. Observational Setup and Calibrators

We observed AT2018cow with the EVN at 1.67 GHz in the first experiment and at 5 GHz in the later four experiments. A total of 21 radio telescopes spreading Africa, Asia, Europe, and USA participated in the observations. These include: Ar (Arecibo 300 m, USA), Bd (Badary 32 m, Russia), Cm (Cambridge 32 m, UK), De (Defford 25 m, UK), Ef (Effelsberg 100 m, Germany), Hh (Hartebeesthoek 26 m, South Africa), Ib (Irbene 32 m, Latvia), Ir (Irbene 16 m, Latvia), Jb2 (Lovell 76 m, UK), Km (Kunming 40 m, China), Kn (Knockin 25 m, UK), Mc (Medicina 25 m, Italy), On85 (Onsala 25 m, Sweden), Sr (Sardinia 64 m, Italy), Sv (Svetloe 32 m, Russia), T6 (Tianma 65 m, China), Tr (Torun 32 m, Poland), Ur (Urumqi 26 m, China), Wb (Westerbork 25 m, Netherlands), Ys (Yebes 40 m, Spain), Zc (Zelenchukskaya 32 m, Russia). The experiment setup details are summarized in Table 1 and include the EVN project code, observation date, observation frequency, time duration, bandwidth, and participating telescopes. The participation of Chinese and Russian telescopes in Sessions 2, 4, and 5 significantly increases the east–west direction resolution to the 1 mas level.

All observations were carried out in the phase-referencing mode. J1619+2247 (≈ 0.6 Jy at 5 GHz, $55'$ away from AT2018cow) was used as the primary calibrator. Its coordinate is α(J2000) = $16^h19^m14\overset{s}{.}8245991$ and δ(J2000) = $22°47'$ $47''\!.851082$ in the source catalog of GSFC 2015a from the NASA Goddard Space Flight Center (GSFC) VLBI group. We observed J1619+2247 and AT2018cow with a cycle of 220 s (40 s on J1619+2247 and 180 s on AT2018cow). In order to further improve the astrometric precision and verify the positional stability of the reference source, we observed two additional sources for a two-minute scan per half hour. They are weaker but closer: NVSS J161541.6+221629 ($4'\!.3$ away from AT2018cow, named R1 hereafter), and NVSS J161640.8 +221856 (angular separation of $9'\!.8$, named R2 hereafter). A bright quasar J1642+3948 (≈ 6 Jy) was observed as the fringe finder.

2.2. Data Processing

The correlation was done by the EVN software correlator SFXC (Keimpema et al. 2015) at Joint Institute for VLBI ERIC (JIVE) using the typical correlation parameters (integration time: 1 s, frequency resolution: 1 MHz). In the eEVN observations of RY007A (Session 1) and EY033A (Session 3), the data were transferred via broadband optical fiber and correlated in real time. The real-time correlation and the rapid distribution of the first session correlated data played a key role in ensuring the successful detection of AT2018cow and verifying the suitability of the two nearby calibrators R1 and R2.

The visibility data were calibrated using the software package Astronomical Image Processing System (AIPS; Greisen 2003) of the National Radio Astronomy Observatory (NRAO). The side channels with low amplitude were dropped out in loading the data. The AIPS task ACCOR was performed to renormalize the visibility amplitude. A priori amplitude calibration was performed with the system temperatures and the antenna gain curves provided by each station. In case some telescope monitoring data were missing, nominal values of the system-equivalent flux density in the EVN status table were used instead. The ionospheric dispersive delays were corrected using a map of total electron content provided by Global Positioning System satellite observations. Phase errors due to antenna parallactic angle variations were removed. After a manual phase calibration and bandpass calibration were carried out using the fringe finder, the global fringe-fitting was performed on the phase-referencing calibrators.

We imaged the calibrator J1619+2247 in the DIFMAP software package (Shepherd et al. 1994). It shows a one-sided core–jet structure with a total flux density of 0.61 ± 0.03 Jy. Its core, i.e., the optically thick jet base, has a flux density of 0.20 ± 0.01 Jy and was used as the reference point in the initial phase-referencing astrometry. The CLEAN component model of J1619+2247 was imported into AIPS, and the fringe-fitting was re-run to eliminate the source structure-dependent phase errors. In the second iteration of the phase-referencing calibration, we imaged R2, which shows a compact source of 19 mJy, and then applied the phase solutions derived from R2 to the data of AT2018cow and R1. Phase-referencing calibration using a closer calibrator in this way may further reduce the astrometric error.

3. Results

3.1. Detection and Flux Density Evolution

The first session 2 hr electronic-EVN (e-EVN) observation at 1.67 GHz on 2018 September 20 ($t_d = 94.4$ day) was aimed at an initial detection, characterizing its compactness and potential suitability for continued monitoring. The experiment successfully detected an unresolved compact source with a flux density of 0.86 ± 0.04 mJy beam^{-1}, thus warranting continued monitoring (An 2018).

The second session was carried out at 5 GHz on two sequential dates on 2018 October 20 ($t_d = 126.2$ day) and 2018 October 21, each lasting 12 hr. The observations were made in disk-recording mode. The preliminary motivation was to resolve the source structure. This session offered the best resolution (synthesized beam size of 2.64 mas × 1.81 mas) and the highest signal-to-noise ratio (S/N of ≈300) based on an image rms noise of 0.016 μJy beam^{-1} after self-calibration. An unresolved source was detected with a peak flux density of 4.80 ± 0.04 mJy beam^{-1}, 5.6 times brighter than that in the first session.

The third session was a 3 hr e-EVN observation at 5 GHz on 2019 February 15 ($t_d = 242.8$ days). The source remains unresolved with a substantially decreased flux density of 0.38 ± 0.03 mJy beam^{-1}. The resulting synthesized beam is 10.4 mas ×1.80 mas, substantially larger than other sessions due to the absence of long east–west baselines.

The fourth session consisting of two 12 hr observations at 5 GHz on 2019 March 5 and 6 was aimed at monitoring the source structure or emission peak change. The source was detected at a peak flux density of 0.23 ± 0.01 mJy beam^{-1}. A fifth session was a 12 hr observation at 5 GHz on 2019 June 5, again aimed at monitoring any structure or emission peak changes. Benefiting from the higher data rate of 2 Gbps, this session has the highest sensitivity. The source was detected despite a vastly decreased flux density of 0.04 ± 0.01 mJy beam^{-1}. The source images from Sessions 2–5 are presented in Figure 1, and the imaging results are summarized in Table 2 and include the observation day, observation frequency, the peak flux density and associated 1σ error, the integrated flux density, the source structural parameters, and the array used.

The 5 GHz light curve in Figure 2 covers the early phase (<20 days), turnover (82.5–132.6 days), and later phase (>132.6 days). The light curve is fitted with a smoothly broken power-law model based on a Markov Chain Monte Carlo (MCMC) method to obtain the temporal indices before and after the break, the "smoothness" of the break, and the associated flux density and time at the break (see Figures 2 and 3; details in Appendix C), yielding a peak flux density of 5.6 mJy at a time of 102.1 days and a steep decline with an index $\leqslant -5.2$.

3.2. Astrometry and Proper Motion

The emission peak is determined by averaging the positions in individual sessions: $\alpha = 16^{\rm h}16^{\rm m}00\overset{\rm s}{.}224169 \pm 0\overset{\rm s}{.}000001$ and $\delta = 22°16'04''.890539 \pm 0''.000012$. The size of the morphologically unresolved source ranges from 0.068 mas in Session 2 to 0.35 mas in Session 5 based on Monte Carlo simulations. From the multiepoch VLBI data spanning 260 days, the proper motion 1 − σ upper limits are constrained to within $\mu_{\alpha\cos\delta} = 0.070 \pm 0.049$ mas yr^{-1} and $\mu_\delta = 0.131 \pm 0.088$ mas yr^{-1} ($\leqslant 0.15 \pm 0.10$ mas yr^{-1} or 0.14 ± 0.10 c). This conclusively rules out a relativistic jet, with a consequent intrinsically luminous expanding afterglow.

3.3. Source Environmental Properties

An analytic model is used to fit the synchrotron emitting afterglow evolution (Granot & Sari 2002), which assumes a self-similar adiabatically expanding ejecta interacting with the surrounding constant density or stratified medium (Blandford & McKee 1976; Gao et al. 2013). Using the best-fitted VLBI size $\theta_A \leqslant 0.068$ mas ($t_d = 126.2$ days) and total energy $E = (0.01 − 0.32) \times 10^{52}$ erg (Margutti et al. 2019), the number density is estimated to be $(0.12 − 8.00) \times 10^5$ cm^{-3} at time $t_d = 22$ days, consistent with the reported 3.0×10^5 cm^{-3} on the same date (Ho et al. 2019). Fractions of particle and magnetic field energy densities are $\epsilon_e = 0.03$–0.04 and $\epsilon_B \geqslant 0.33$, respectively. As ϵ_B is larger than ϵ_e by an order of magnitude, this suggests a highly magnetized medium with $B \geqslant 0.84$ G, calculated assuming that the magnetic field energy density in the comoving frame is a fraction ϵ_B of the total energy density ϵ, i.e., $B^2/(8\pi) = \epsilon_B\epsilon$; see Appendix E. This independent estimate during the optically thin declining phase is consistent with the inferred $B \approx 6$ G based on the expanding optically thick phase (Ho et al. 2019). Submillimeter polarimetric observations report the nondetection of linear polarization ($\leqslant 0.15\%$), attributable to Faraday depolarization
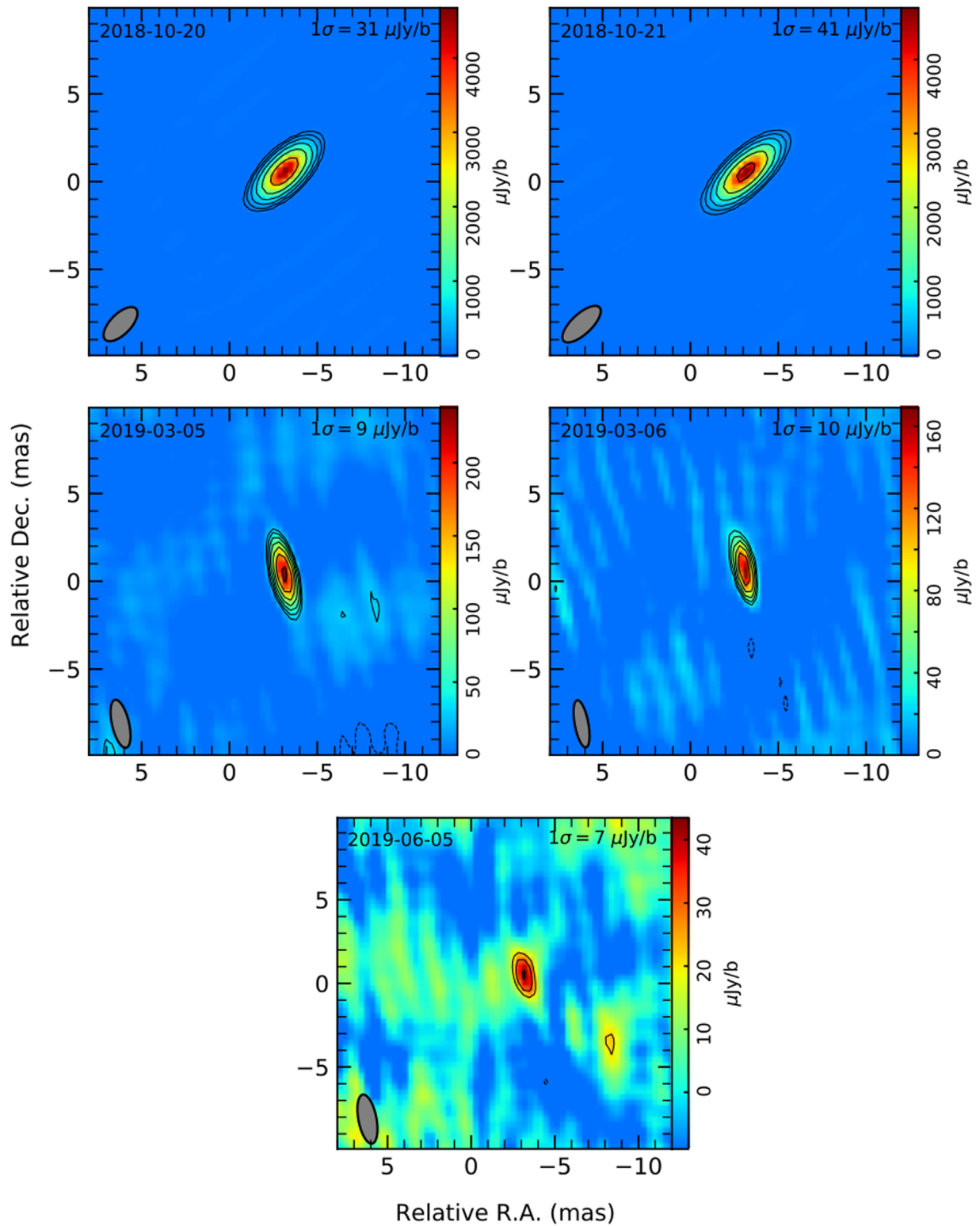
Figure 1. High-resolution 5 GHz VLBI images of AT2018cow during Sessions 2, 4, and 5 indicating a compact, unresolved, and fading transient. The observation date is in the top left corner, the image noise threshold is in the top right corner and the restoring beam shape (and size) are depicted in the bottom left corner. The color scale represents the intensity (in units of μJy beam^{-1}) with the lowest shown in blue and the highest shown in red.

in a dense and strongly magnetized medium (Huang et al. 2019). The consistency of our independent measurements confirms the validity of the dense magnetized medium surrounding the transient and suggest that this environment persists well into the transient evolutionary phase.

4. Discussion

The expected number density is $1\,\mathrm{cm}^{-3}$ and magnetic field strength is $1\,\mu$G in the tidal disruption scenario (Huang et al. 2019). The inferred dense, magnetized medium and the steeply declining flux density thus disfavor this scenario. The scenario

Table 2
The EVN Phase-referencing Imaging Results of AT2018cow

Session	MJD (day) (1)	t_{post} (day) (2)	ν_{obs} (GHz) (3)	S_{peak} (mJy beam^{-1}) (4)	σ_{map} (mJy beam^{-1}) (5)	S_{int} (mJy) (6)	ϕ_{maj} (mas) (7)	ϕ_{min} (mas) (8)	ϕ_{pa} (deg) (9)	Array (10)
1	58379.8	94.4	1.67	0.86	0.040	0.89	48.3	15.0	+45.1	e-EVN
2	58411.6	126.2	4.99	4.79	0.031	4.67	2.64	1.81	+08.9	Full EVN
	58412.6	127.2	4.99	4.80	0.041	4.72	2.59	2.08	+09.3	Full EVN
3	58528.2	242.8	4.93	0.38	0.026	0.37	10.4	1.80	+78.8	e-EVN
4	58547.2	261.8	4.99	0.27	0.009	0.24	2.81	0.97	+13.1	Full EVN
	58548.2	262.8	4.99	0.19	0.010	0.17	2.73	0.78	+10.6	Full EVN
5	58640.0	354.6	4.93	0.043	0.007	0.043	2.97	1.04	+11.4	Full EVN

Note. Columns give (1) Modified Julian Date (MJD), (2) post-explosion day (reference time: MJD 58285.4); (3) central observing frequency; (4) peak brightness in mJy beam^{-1} in the dirty map; (5) off-source image noise level; (6) total flux density derived by fitting the visibility data to a point-source model; (7)–(9) the major axis, the minor axis, and the position angle of the elliptical Gaussian beam synthesized with natural weighting; and (10) network configuration. Note that the nominal systematic errors due to visibility amplitude calibration for S_{peak} and S_{int} are $\sim$5%.
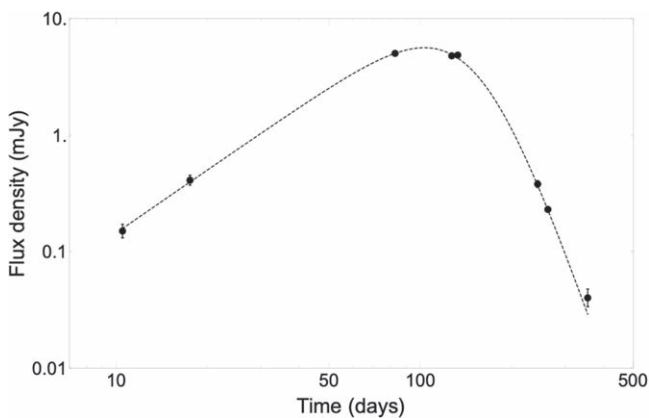
Figure 2. MCMC fitting of the 5 GHz light curve of AT2018cow gives a steep declining phase slope of -7.5 ± 1.1. A smoothly broken power-law fit (see Appendix C for the light-curve fitting methods adopted) gives a break flux density $F_{\nu,p}$ of $3.36^{+0.60}_{-0.77}$ mJy, break time t_p of $151.09^{+14.75}_{-10.36}$ days, and temporal indices before and after the break α_1 and α_2 of $1.81^{+0.07}_{-0.06}$ and $-7.45^{+0.90}_{-1.30}$, respectively, and smoothness parameter governing the peak turnover s of $0.39^{+0.10}_{-0.09}$. These correspond to a peak flux density of 5.6 ± 1.4 mJy at a time of 102.1 ± 13.1 days.

of a failed explosion of a giant star that results in the direct collapse of the core to an accreting black hole is disfavored owing to the fall-back accretion-powered light curve expected to decline with an index $\geqslant -2.4$ (Metzger et al. 2018). A neutron star powered central engine is disfavored owing to the expected magnetic field strength in the shocked environment of $\sim 10^4$ G (4 orders of magnitude higher than we infer, using the expressions for the equipartition magnetic field strength in Appendix E; Lyutikov & Toonen 2019). We thus favor a scenario involving the successful supernova of a low-mass star that results in a newly formed magnetar powering the transient, as was speculated in literature (Prentice et al. 2018; Fang et al. 2019; Ho et al. 2019) based on new, independent constraints from the VLBI observations during the late phase of transient evolution that substantiate this interpretation. The observations and implications in this context are further developed below.

For a fast spinning magnetar of period 10 ms with a surface magnetic field strength $B_{15} = B/(10^{15}$ G$)$, the rotational energy $E_R \approx 2 \times 10^{50}$ erg can potentially be lost to the surrounding medium through dipole radiation over a spin-down timescale

$t_s = 5.3$ days. The ejecta from the supernovae can radiate this energy over a diffusion timescale $t_D = 3.8$ days, resulting in a peak luminosity $L_p \approx 9.3 \times 10^{44}$ erg s^{-1}, which then decays as t^{-2} (Kasen & Bildsten 2010). The equipartition magnetic field strength in the surrounding medium (Lyutikov & Toonen 2019) ranges between $B_{eq} = 0.07$–0.5 G at $t_d = t_p$ considering the cases of a wind-driven shock and the shock propagating through the low-mass stellar ejecta. This is consistent within an order of magnitude of $B \geqslant 0.84$ G, estimated above for the afterglow, supporting the scenario involving the magnetar driven winds causing the observed extremely luminous transient.

The rapidly declining light curve ($\alpha_2 \leqslant -5.2$) challenges the presented scenario. Assuming (i) a rapid transition of the blastwave to the Newtonian expanding phase, where the swept-up mass from the surrounding environment equals that in the initial ejecta (Gao et al. 2013; ≈ 0.1–$0.4\, M_\odot$), and (ii) a density contrast of 0.01 between the material immediately in the vicinity of the blastwave and that far away, the expected flux density can decline as -4.8 (Kumar & Panaitescu 2000), possibly explaining this observational challenge.

An interesting consequence is the production of fast radio bursts (FRBs) from the magnetar interaction with the magnetized environment (Murase et al. 2016; Metzger et al. 2017, 2019). This may provide a new understanding of FRBs, especially as three of these, the repeating FRB 121102 (Chatterjee et al. 2017), FRB 190523 (Ravi et al. 2019), and FRB 180924 (Bannister et al. 2019), have been precisely localized so far with a putative magnetar origin. The VLBI technique thus offers a promising, novel manner of understanding properties of transients (progenitor and evolution) as evidenced from the presented direct imaging observations of an FBOT.
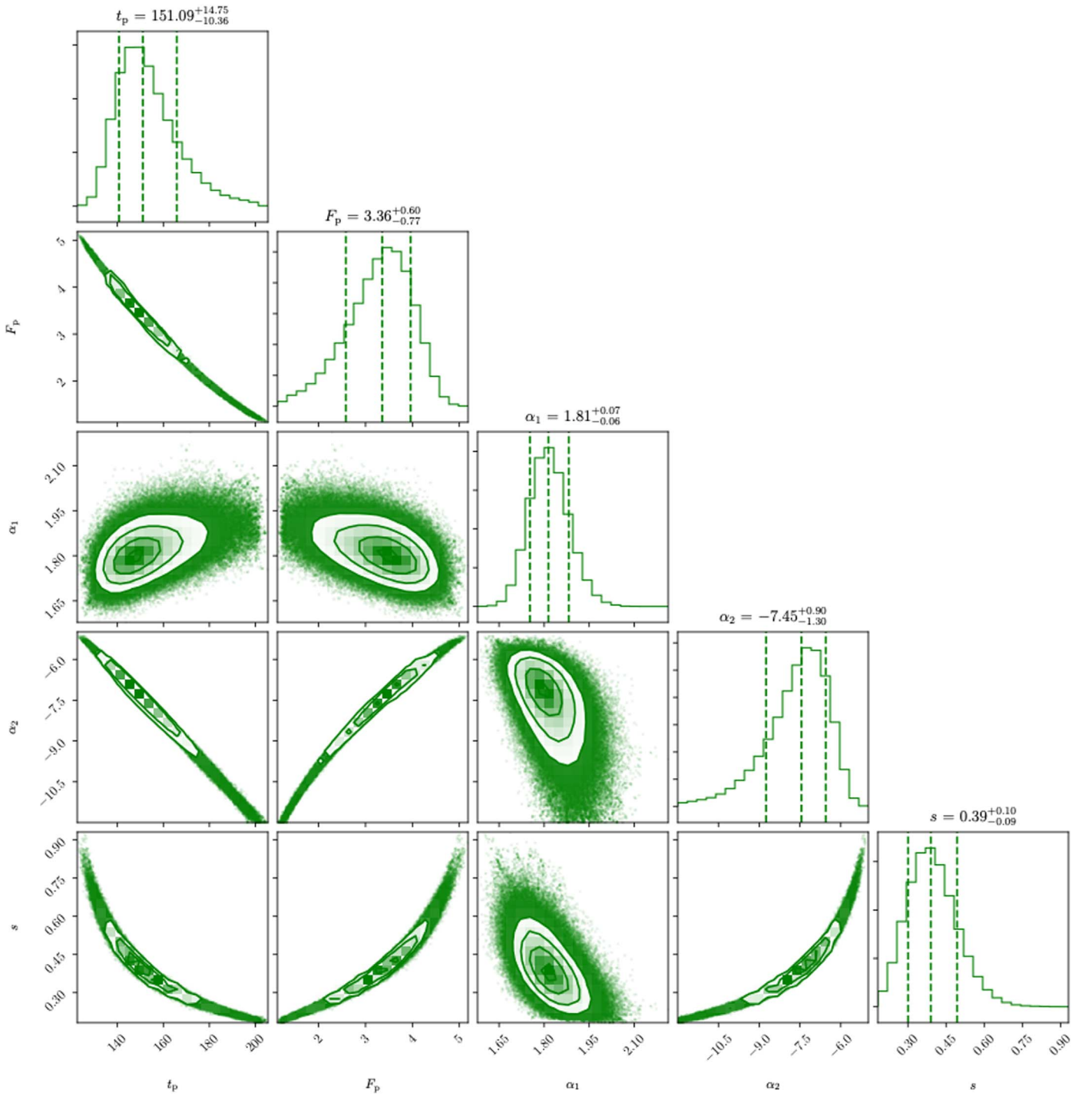
Figure 3. Corner plot showing the MCMC fitting results. A smoothly broken power-law fit (see Appendix C for the light-curve fitting methods adopted) gives a break flux density $F_{\nu,p}$ of $3.36^{+0.60}_{-0.77}$ mJy, break time t_p of $151.09^{+14.75}_{-10.36}$ days, and temporal indices before and after the break α_1 and α_2 of $1.81^{+0.07}_{-0.06}$ and $-7.45^{+0.90}_{-1.30}$, respectively, and smoothness parameter governing the peak turnover s of $0.39^{+0.10}_{-0.09}$. The MCMC propagates both direct and covariance based errors in these estimates and does not require prior knowledge of their underlying statistical distributions.

Appendix A
VLBI Observational Results

A morphologically compact unresolved mas-scale radio source is unambiguously detected in AT2018cow in all epochs. The flux densities of AT2018cow and the related image parameters are listed in Table 2. We should note that σ_{map} only represents the random fluctuations in the image, i.e., the rms noise. An additional 5% systematic error of the flux density

Table 3
The Astrometric Results and the Constraints on the Size of AT2018cow

MJD (day)	R.A. α(J2000)	σ_α (mas)	Decl. δ(J2000)	σ_δ (mas)	θ_{sim} (mas)	$T_{b,min}$ (K)
58411.6	$16^h16^m00^s2241686$	0.0017	$22°16'04''890567$	0.0025	0.068, 0.12, 0.14	1.2×10^{10}
58412.6	$16^h16^m00^s2241686$	0.0021	$22°16'04''890511$	0.0026	0.064, 0.13, 0.16	9.2×10^{9}
58547.2	$16^h16^m00^s2241700$	0.021	$22°16'04''890412$	0.049	0.19, 0.31, 0.35	9.7×10^{7}
58548.2	$16^h16^m00^s2241728$	0.026	$22°16'04''890652$	0.075	0.22, 0.39, 0.47	3.8×10^{7}
58640.0	$16^h16^m00^s2241652$	0.093	$22°16'04''890460$	0.23	0.35, 0.76, 1.42	1.1×10^{6}

Note. Columns give (1) MJD, (2)–(3) R.A. and 1σ formal uncertainty (systematic uncertainty: 0.022 mas), (4)–(5) decl. and 1σ formal uncertainty (systematic uncertainty: 0.025 mas), (6) sizes at the cumulative probabilities of 68.3%, 95.4%, 99.7% from Monte Carlo simulation of a fake point source, (7) the lower limit of the brightness temperature.

measurements is included in the calibration of the visibility amplitude.

There is no hint of any secondary component or extension in the residual images at any session with diverse (u, v) coverages and dynamic ranges. The total flux density fitted with a point-source model is consistent with the peak flux density in the dirty map, supporting the detection of an extremely compact source. In order to estimate the source size in such an unresolvable case, we performed 1000 Monte Carlo simulations: in each simulation, we first subtracted the observed source AT2018cow from the visibility data, then we added a point source with the same flux density as that of AT2018cow at a random position, next we fitted the fake source with a circular Gaussian model. The sizes at the cumulative probabilities of 68.3%, 95.4%, and 99.7% are reported in column 6 in Table 3, and the minimum brightness temperature based on the size constraint at 99.7% in column 7. Sessions 1 and 3 resulted in larger beam sizes due to missing long baselines; therefore, they are not included in this estimate.

Appendix B
Astrometry and Proper Motion

R2 shows a compact structure (angular size ≈0.3 mas) and a flux density of 18.9 ± 1.0 mJy at 5 GHz and 15.6 ± 0.8 mJy at 1.67 GHz. We measured its position: α(J2000) = $16^h16^m40^s8140683$, δ(J2000) = $22°18'56''410927$ (J2000) from the first full EVN observation in Session 2. Comparing the peak positions in all sessions results in a formal positional uncertainty of only a few microarcseconds (μas). Then we derived a weighted average position of AT2018cow: α(J2000) = $16^h16^m00^s224169 \pm 0^s000001$ and δ(J2000) = $22°16'04''890539 \pm 0''000012$. As the primary calibrator J1619 +2247 comprises an elongated jet with a flux density of 0.41 ± 0.02 Jy, which may give rise to a systematic positional uncertainty up to 0.8 mas. In order to avoid this systematic uncertainty of the absolute position, we focus on the differential astrometry, i.e., the relative motion between R2 and AT2018cow, in the following discussion. Only the formal position uncertainty is taken into account.

R1 is used as a checker source to evaluate the phase-referencing quality. R1 is successfully detected in the dirty image without any self-calibration with an S/N ≈ 100. It has a flux density of 15.1 ± 0.8 mJy at 5 GHz and 23.8 ± 1.2 mJy at 1.67 GHz, respectively. The source shows a resolved structure consisting of two components. The brighter and more compact component is most likely the core. In Session 2, we found some phase errors on the baselines associated with Ibbene and Arecibo. Thus, the two

data of these two stations were excluded from the astrometric study. With respect to R2, the statistical average position of R1 is α(J2000) = $16^h15^m41^s6911175 \pm 0.0000015$, δ(J2000) = $22°16'28''222084 \pm 0.000025$. Since both AT2018cow and R1 have similar angular distances, 9′.8 and 13′.9, to R2, respectively, and their data were calibrated in the same way, their systematic position errors are expected to be roughly the same. Thus, the astrometric accuracy is mainly associated with the position accuracy of R2.

Figure 4 shows the astrometric results from the full EVN observations (Sessions 2, 4, and 5) involving more telescopes. As the transient faded significantly in Sessions 4 and 5, the error bars and ellipses became much bigger. Using the software PMPAR,[4] we estimated a proper motion of $\mu_{\alpha\cos\delta} = 0.070 \pm 0.049$ mas yr^{-1} and $\mu_\delta = -0.131 \pm 0.088$ mas yr^{-1}. The fitted proper motions only account for 1.5σ, and yet suggest no significant proper motion in AT2018cow.

Appendix C
Light-curve Fitting

The 5 GHz light curve in Figure 2 is compiled from reported and measured flux densities covering the early phase (<20 days), turnover (82.5–132.6 days; including our Session 2), and later phase (≈132.6 days; including our Sessions 3–5). The light curve is fitted with a smoothly broken power-law model $F_\nu = 2^{1/s}F_{\nu,p}((t/t_p)^{-s\alpha_1} + (t/t_p)^{-s\alpha_2})^{-1/s}$, where $F_{\nu,p}$ is the break flux density (mJy), t_p is the break time (day), α_1 and α_2 are the temporal indices before and after the break, respectively, and s is a smoothness parameter governing the peak turnover. A least-squares fitting gives $(\alpha_1, \alpha_2, s) = (1.7 \pm 0.1, -5.2 \pm 0.2, 0.9 \pm 0.1)$. With a $(F_{\nu,p}, t_p) = (5.0 \pm 0.1$ mJy, 124.4 ± 1.4 days), we estimate a peak flux density of 5.9 ± 0.1 mJy at a time of 103.3 ± 1.9 days.

The slope $\alpha_2 = -5.2 \pm 0.2$ derived from the least-squares fitting is much steeper than other known transients. We then employed a Markov Chain Monte Carlo (MCMC) method (emcee Python package; Foreman-Mackey et al. 2013) to better constrain these parameters without any prior knowledge of their underlying statistical distributions. The MCMC results are shown in the corner plot of Figure 3 and are $(\alpha_1, \alpha_2, s) = (1.81^{+0.07}_{-0.06}, -7.45^{+0.90}_{-1.30}, 0.39^{+0.10}_{-0.09})$. With a $(F_{\nu,p}, t_p) = (3.36^{+0.60}_{-0.77}$ mJy, $151.09^{+14.75}_{-10.36}$ days), we estimate a peak flux density of 5.6 ± 1.4 mJy at a time of 102.1 ± 13.1 days. As MCMC results in an even steeper slope of $\alpha_2 = -7.45^{+0.90}_{-1.30}$,

---

[4] https://github.com/walterfb/pmpar
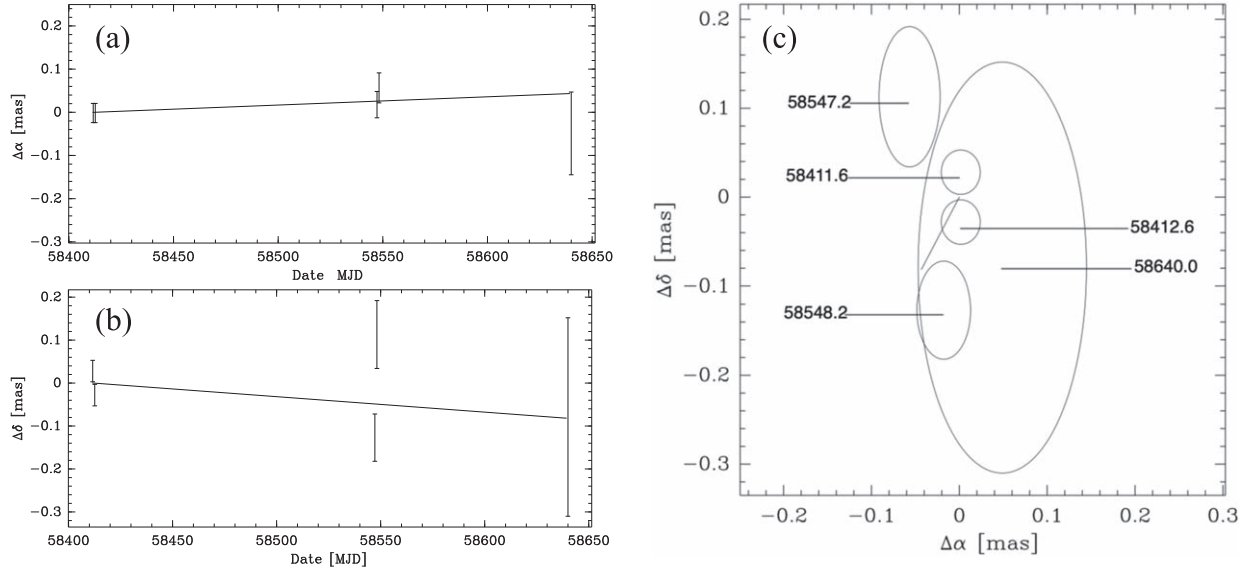
Figure 4. No significant proper motion of AT2018cow. (a) Plot of the position offset in R.A. vs. time. (b) Plot of the position offset in decl. vs. time. (c) The scatter plot of the measured position offsets. All the error bars and ellipses represent 1σ uncertainties and the epochs corresponding to the appropriate session are listed in MJD. The straight lines in panels (a) and (b) represent the proper motion searching results: $\mu_{\alpha\cos\delta} = 0.070 \pm 0.049$ mas yr^{-1} and $\mu_{\delta} = -0.131 \pm 0.088$ mas yr^{-1}.

Table 4
The Model Fitting Parameters for the 5 GHz Light Curve

Fitting Method	$F_{\nu,p}$ (mJy)	t_p (days)	α_1	α_2	s
Chi-square	5.0 ± 0.1	124.4 ± 1.4	1.7 ± 0.1	-5.2 ± 0.2	0.9 ± 0.1
MCMC	3.4 ± 0.7	151.1 ± 12.8	1.8 ± 0.1	-7.5 ± 1.1	0.4 ± 0.1

Note. Column (1) is the method used to fit the light curve, columns (2)–(6) are the results of the fitting along with their corresponding 1σ errors.

the true slope is taken to be $\leqslant -5.2$. The fitting results are summarized in Table 4.

Appendix D
Afterglow Spectral Evolution

The source size, flux density, and light-curve fitting parameters are used in an analytic model depicting the synchrotron emitting afterglow evolution (Granot & Sari 2002). The model assumes a self-similar adiabatically expanding ejecta interacting with the surrounding medium (Blandford & McKee 1976; Gao et al. 2013) in two scenarios. The first (Model 1) is characterized by a medium of constant density n_0. The second (Model 2) is characterized by a stratified wind-like medium with a density profile $A_* r^{-2}$, where A_* is an effective measure of the mass density, and r is the radial distance from the central core. The current data are not able to distinguish between these two models; therefore, we make the subsequent calculations in both scenarios.

Associated emission frequencies mark distinctive breaks in the evolving synchrotron spectrum, corresponding to transitions from fast-cooling ($\nu_c < \nu_m$) to slow-cooling ($\nu_m < \nu_a$) phase. ν_a is the synchrotron self-absorption frequency characterizing a surface whose optical depth to synchrotron self-absorption is unity, ν_m is the synchrotron frequency emitted by

the power-law distributed electrons, and ν_c is the synchrotron frequency of an electron that cools over the dynamic timescale.

D.1. Model 1 (Constant Density Interstellar Medium)

The synchrotron frequency ν_m and synchrotron self-absorption frequency ν_a are

$$\nu_m = (1.58 \times 10^{13} \text{ Hz})E_{52}^{1/2}\epsilon_e^2\epsilon_B^{1/2}t_d^{-3/2}$$
$$\nu_a = (4.67 \times 10^{11} \text{ Hz})E_{52}^{0.24}n_0^{0.13}\epsilon_e^{0.46}\epsilon_B^{0.12}t_d^{-0.73}. \quad (1)$$

With $\phi_m = (\nu/\nu_m)$, the corresponding composite spectrum as a function of the observation frequency ν (in GHz) is given by

$$F_\nu = F_{\nu,\max}(\phi_m^2 e^{-8.22\phi_m^{2/3}} + \phi_m^{5/2})(1 + (\nu/\nu_a)^{2.14})^{-1.82}$$
$$F_{\nu,\max} = (1.89 \times 10^{10} \text{ mJy})E_{52}^{3/2}n_0^{-1/2}\epsilon_e^5\epsilon_B t_d^{-5/2}. \quad (2)$$

D.2. Model 2 (Stratified Interstellar Medium)

The synchrotron frequency ν_m and synchrotron self-absorption frequency ν_a are

$$\nu_m = (2.54 \times 10^{13} \text{ Hz})E_{52}^{1/2}\epsilon_e^2\epsilon_B^{1/2}t_d^{-3/2}$$
$$\nu_a = (6.73 \times 10^{11} \text{ Hz})E_{52}^{0.12}A_*^{0.26}\epsilon_e^{0.46}\epsilon_B^{0.12}t_d^{-0.86}. \quad (3)$$

The corresponding composite spectrum as a function of the observation frequency ν (in GHz) is given by

$$F_\nu = F_{\nu,max}(\phi_m^2 e^{-8.56\phi_m^{2/3}} + \phi_m^{5/2})(1 + (\nu/\nu_a)^{2.31})^{-2.03}$$

$$F_{\nu,max} = (1.54 \times 10^{10} \text{ mJy})E_{52}^2 A_*^{-1} \epsilon_e^5 \epsilon_B t_d^{-2}.$$

(4)

Model parameters include the explosion energy $E_{52} = E/(10^{52} \text{ erg s}^{-1})$, number density of the surrounding medium (n_0 in Model 1, or $A_* r^{-2}$ in Model 2), and fractions of the shock energy density in the particles ϵ_e and magnetic fields ϵ_B. The source angular size is related to E_{52}, n_0 or A_*, t_d by $\theta_{A1} = (0.83 \text{ mas})E_{52}^{1/4} n_0^{-1/4} t_d^{1/4}$ (Model 1) and $\theta_{A2} = (0.32 \text{ mas})E_{52}^{1/2} A_*^{-1/2} t_d^{1/2}$ (Model 2). Using the best-fitted VLBI size θ_A(epoch 2) $\leqslant 0.07$ mas ($t_d = 126.2$ days) and $E_{52} = 0.01$–0.32 (Margutti et al. 2019), we obtain $n_0 = (2.5–80.0) \times 10^4 \text{ cm}^{-3}$ for Model 1, and $A_* = 26.3$–842.1 for Model 2 corresponding to a number density $n = (1.2–39.0) \times 10^4 \text{ cm}^{-3}$ at an observation time $t_d = 22$ days. These estimates are consistent with the reported $3.0 \times 10^5 \text{ cm}^{-3}$ on $t_d = 22$ days (Ho et al. 2019), confirming a dense surrounding medium in AT2018cow.

Appendix E
Physical Conditions in the Surrounding Medium and Implications on the Progenitor

The model flux density $F_\nu(E_{52}, n_0 \text{ or } A_*, \epsilon_e, \epsilon_B, t_d)$ when subject to the conditions $F_\nu(t_d = t_p) = F_{\nu,p}$ and $F'_\nu(t_d = t_p) = 0$ yields $\epsilon_e = 0.03$–0.04 and $\epsilon_B \geqslant 0.33$, suggesting a magnetically dominated medium. For the magnetic field energy density (in the comoving frame) being a fraction ϵ_B of the total energy density $\epsilon = 4\gamma^2 n m_p c^2$, i.e., $B^2/(8\pi) = \epsilon_B \epsilon$, this corresponds to $B_1 = (1.43 \text{ G})E_{52}^{1/8} n_0^{3/8} \epsilon_B^{1/2} t_d^{-3/8}$ (Model 1) and $B_2 = (1.45 \text{ G})E_{52}^{-1/4} A_*^{3/4} \epsilon_B^{1/2} t_d^{-3/4}$ (Model 2), based on $\gamma_1 = 3.67 E_{52}^{1/8} n_0^{-1/8} t_d^{-3/8}$ (Model 1) and $\gamma_2 = 3.72 E_{52}^{1/4} A_*^{-1/8} t_d^{-1/4}$ (Model 2). Using the above parameters and assuming t_d as the peak time, we get $B_1 \geqslant 3.42$ G (Model 1) and $B_2 \geqslant 0.84$ G (Model 2).

The magnetar scenario is now explored further to estimate the energetics (Kasen & Bildsten 2010) and magnetic field strength in the medium (Lyutikov & Toonen 2019). The moment of inertia of the magnetar $I = (2/5)MR^2 = 1.1 \times 10^{45} \text{ g cm}^2$ assuming a mass $M = 1.4 M_\odot$ and radius $R = 10$ km. With magnetar spin period $P_{-2} = P/(10 \text{ ms})$, the rotational energy available is $E_R = 2\pi^2 I \ P^{-2} = (2.2 \times 10^{50} \text{ erg})P_{-2}^{-2}$. For a magnetar with a surface magnetic field strength $B_{15} = B/(10^{15} \text{ G})$, this energy can potentially be lost to the surrounding medium through dipole radiation over the spin-down timescale $t_s = 3Ic^3P^2(2\pi^2 B^2 R^2)^{-1} = (5.3 \text{ days})B_{15}^{-2} P_{-2}^2$. The adiabatically expanding ejecta slows down upon emitting a bulk of this energy over the diffusion timescale $t_D = (\kappa M_{ej}/(4v_{ej}c))^{1/2} = 3.8$ days assuming a diffusion coefficient $\kappa = 0.2 \text{ g}^{-1} \text{ cm}^2$, an ejecta mass $M_{ej} = 0.3 \ M_\odot$, and a velocity $v_{ej} = 0.1 \ c$. This results in a peak luminosity $L_p \approx E_R t_s/t_D^2 = (9.3 \times 10^{44} \text{ erg s}^{-1})B_{15}^{-2}$.

The luminosity then decays as a power law $L = L_p(1 + t/t_s)^{-2}$ (Margutti et al. 2019) based on which the equipartition magnetic field strength in the surrounding medium for a wind-driven shock (Lyutikov & Toonen 2019) is $B_{eq} = (4.9 \times 10^3 \text{ G})B_{15}^{-1/2} t_d^{-5/4}(1 + t_d/t_s)^{-1}$ for the shock propagating through the ejecta (assuming an ejecta mass $M_{ej} = 0.3 \ M_\odot$ and a velocity $v_{ej} = 0.1 \ c$), and $B_{eq} = (2.1 \times 10^2 - 1.2 \times 10^3 \text{ G})t_d^{-1}(1 + t_d/t_s)^{-1}$ for the shock propagating through the pre-explosion wind. In the latter case, we use $\dot{M}/v_w = (1.66 \times 10^{14} - 5.31 \times 10^{15}) \text{ g cm}^{-1}$ based on the inferred $A_* = 26.3$–842.1 constrained from the VLBI size of the source. For t_d being the peak time, $B_{eq} = 0.07$–0.5 G in both cases, consistent to within an order of magnitude of the estimate made above of B_2 (and $B_1) \geqslant 0.84$ G, providing support to the scenario involving the magnetar driven winds causing the observed extremely luminous transient. For the case of a regular neutron star with $B = 10^9$ G, the magnetic field strength in the shock can be as high as $B_{eq} = 1.2 \times 10^4$ G, much higher than the estimate made here, providing considerably less support to scenarios involving a neutron star such as that in a common envelope.

ORCID iDs

P. Mohan ⬥ https://orcid.org/0000-0002-2211-0660
T. An ⬥ https://orcid.org/0000-0003-4341-0029
J. Yang ⬥ https://orcid.org/0000-0002-2322-5232

References

An, T. 2018, ATel, 12067, 1
An, T., Wu, X.-P., & Hong, X. 2019, NatAs, 3, 1030
Bannister, K. W., Deller, A. T., Phillips, C., et al. 2019, Sci, 365, 565
Bietenholz, M. F., Margutti, R., Coppejans, D., et al. 2020, MNRAS, 491, 4735
Blandford, R. D., & McKee, C. F. 1976, PhFl, 19, 1130
Chatterjee, S., Law, C. J., Wharton, R. S., et al. 2017, Natur, 541, 58
Drout, M. R., Chornock, R., Soderberg, A. M., et al. 2014, ApJ, 794, 23
Fang, K., Metzger, B. D., Murase, K., et al. 2019, ApJ, 878, 34
Foreman-Mackey, D., Hogg, D. W., Lang, D., et al. 2013, PASP, 125, 306
Gao, H., Lei, W.-H., Zou, Y.-C., et al. 2013, NewAR, 57, 141
Ghirlanda, G., Salafia, O. S., Paragi, Z., et al. 2019, Sci, 363, 968
Granot, J., & Sari, R. 2002, ApJ, 568, 820
Greisen, E. W. 2003, Information Handling in Astronomy—Historical Vistas, Astrophysics and Space Science Library, Vol. 285 (Dordrecht: Kluwer)
Ho, A. Y. Q., Phinney, E. S., Ravi, V., et al. 2019, ApJ, 871, 73
Huang, K., Shimoda, J., Urata, Y., et al. 2019, ApJL, 878, L25
Inserra, C. 2019, NatAs, 3, 697
Kasen, D., & Bildsten, L. 2010, ApJ, 717, 245
Keimpema, A., Kettenis, M. M., Pogrebenko, S. V., et al. 2015, ExA, 39, 259
Kuin, N. P. M., Wu, K., Oates, S., et al. 2019, MNRAS, 487, 2505
Kumar, P., & Panaitescu, A. 2000, ApJL, 541, L51
Lyutikov, M., & Toonen, S. 2019, MNRAS, 487, 5618
Margutti, R., Metzger, B. D., Chornock, R., et al. 2019, ApJ, 872, 18
Metzger, B. D., Beniamini, P., & Giannios, D. 2018, ApJ, 857, 95
Metzger, B. D., Berger, E., & Margalit, B. 2017, ApJ, 841, 14
Metzger, B. D., Margalit, B., & Sironi, L. 2019, MNRAS, 485, 4091
Murase, K., Kashiyama, K., & Mészáros, P. 2016, MNRAS, 461, 1498
Perley, D. A., Mazzali, P. A., Yan, L., et al. 2019, MNRAS, 484, 1031
Prentice, S. J., Maguire, K., Smartt, S. J., et al. 2018, ApJL, 865, L3
Pursiainen, M., Childress, M., Smith, M., et al. 2018, MNRAS, 481, 894
Ravi, V., Catha, M., D'Addario, L., et al. 2019, Natur, 572, 352
Rivera Sandoval, L. E., Maccarone, T. J., Corsi, A., et al. 2018, MNRAS, 480, L146
Shepherd, M. C., Pearson, T. J., & Taylor, G. B. 1994, BAAS, 26, 987
Smartt, S. J., Clark, P., Smith, K. W., et al. 2018, ATel, 11727, 1
Soker, N., Grichener, A., & Gilkis, A. 2019, MNRAS, 484, 4972
Taylor, G. B., Frail, D. A., Berger, E., et al. 2004, ApJL, 609, L1
Wright, E. L. 2006, PASP, 118, 1711
Yang, J., Paragi, Z., van der Horst, A. J., et al. 2016, MNRAS, 462, L66